iScience

CellPress
OPEN ACCESS

Article

Drive circuitry of an electric vehicle enabling rapid heating of the battery pack at low temperatures

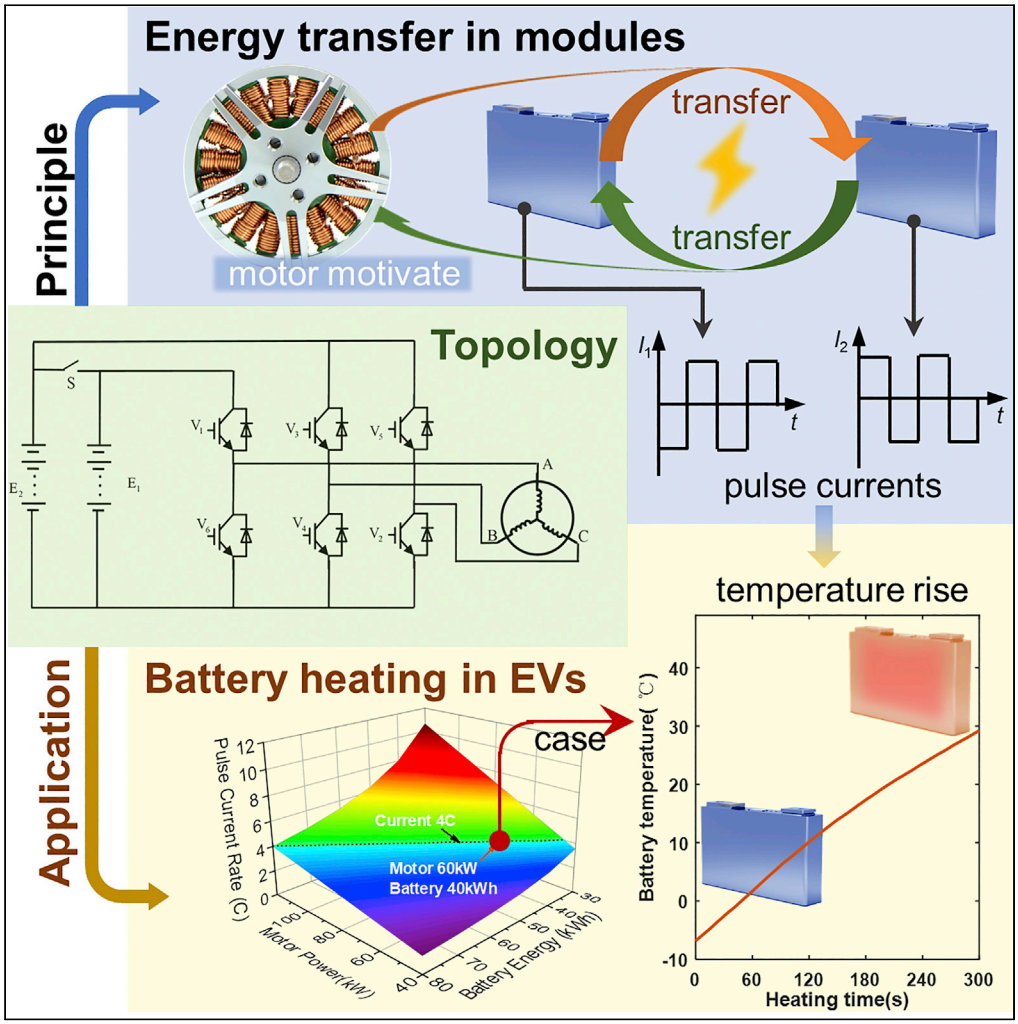

Yalun Li, Xinlei Gao, Yudi Qin, ..., Languang Lu, Xuebing Han, Minggao Ouyang

ouymg@tsinghua.edu.cn

Highlights

Rapid temperature rise, high efficiency, and low cost for battery heating are obtained

The batteries are divided into two modules and connected to the inverter individually

The electricity transferred between battery modules is motivated by a static motor

The pulse currents for battery heating are improved significantly at any frequency

Li et al., iScience 24, 101921
January 22, 2021
https://doi.org/10.1016/j.isci.2020.101921

iScience

CellPress
OPEN ACCESS

Article

Drive circuitry of an electric vehicle enabling rapid heating of the battery pack at low temperatures

Yalun Li,[1] Xinlei Gao,[1,2] Yudi Qin,[1] Jiuyu Du,[1] Dongxu Guo,[1,3] Xuning Feng,[1] Languang Lu,[1] Xuebing Han,[1] and Minggao Ouyang[1,4,*]

Summary

Heating battery at low temperatures is fundamental to avoiding the range anxiety and the time-consuming charging associated with electric vehicles (EVs). One method for achieving fast and uniform battery heating is to polarize the cell under pulse currents. However, the on-board implementation of this method leads to an increase in the cost and size. Therefore, in this study, an adapted EV circuitry compatible with the existing one and an optimized operating condition are proposed to enable rapid battery heating. With this circuit, electricity transfer between the cells can be realized through a motor, leading to remarkably higher battery currents than those of the conventional circuit. The increase in the maximum heating currents (from 1.41C to 4C) resulted in a battery temperature rise of 8.6°C/min at low temperatures. This heating method exhibits low cost, high efficiency, and negligible effects on battery degradation, practical and promising on battery heating of EVs.

Introduction

An essential step toward creating a sustainable society is the adoption of electric vehicles (EVs) in human transportation (Figueres et al., 2017). The dominant power source of EVs is a lithium-ion battery (LIB), which exhibits a high energy density and long lifetime (Goodenough, 2015). However, some practical difficulties associated with LIBs, especially their deteriorated performance under cold environments, have not yet been addressed (Lu et al., 2013; Ren et al., 2019). At extreme temperatures, the driving range of EVs powered by LIBs decreases by 60% and their lifetime shortens (Zhang, Xu and Jow, 2003; Ji et al., 2013; Han et al., 2019). In addition, battery charging at low temperatures may result in lithium plating, diminishing the battery safety (Waldmann et al., 2018; Tomaszewska et al., 2019; Li et al., 2019b). Considerable efforts, including the electrochemical performance improvement (Herreyre et al., 2001; Xu et al., 2019) and operation condition management (López-Ibarra et al., 2020; Yang et al., 2020; Li et al., 2021), have been devoted to overcome these challenges faced by LIBs. For this purpose, the preheating of EV batteries is an effective approach owing to its easy implementation.

The method of battery preheating can be classified, based on the location of the heat source, into internal or external heating (Ji and Wang, 2013; Wu et al., 2020). In external heating, the heat is generated from outside of the batteries. This method can be conveniently implemented for EVs, as multiple options of heat source, including the electric resistances or motor, are available. Furthermore, the heat can be transferred to the battery cells through air, a liquid, or a plate. However, this method suffers from limited heating speed and large energy loss because of long-distance heat conduction or convection (Vlahinos and Pesaran, 2002). In contrast, in the internal heating, the heat source is located inside the cells; therefore, the time delay and energy loss caused by heat conduction can be substantially reduced (Pesaran and Vlahinos, 2003). In particular, internal heating can be achieved by embedding a nickel foil inside a battery case (Wang et al., 2016). In this scenario, the temperature of the batteries increases by 30°C within tens of seconds and the energy loss reduces (Yang et al., 2018). However, under the application of this method, the temperature of the battery structure may become heterogeneous; furthermore, this method cannot be easily applied to existing batteries (Grandjean et al., 2017).

The internal warming of batteries via voltage polarization is a promising approach to achieve rapid and uniform heating (Zuniga et al., 2015). Under alternate current (AC), lithium ions are transferred between the

[1]State Key Laboratory of Automotive Safety and Energy, Tsinghua University, Beijing 100084, China

[2]School of Transportation Science and Engineering, Beihang University, Beijing 10191, China

[3]Department of Automation, Tsinghua University, Beijing 100084, China

[4]Lead contact

*Correspondence: ouymg@tsinghua.edu.cn

https://doi.org/10.1016/j.isci.2020.101921

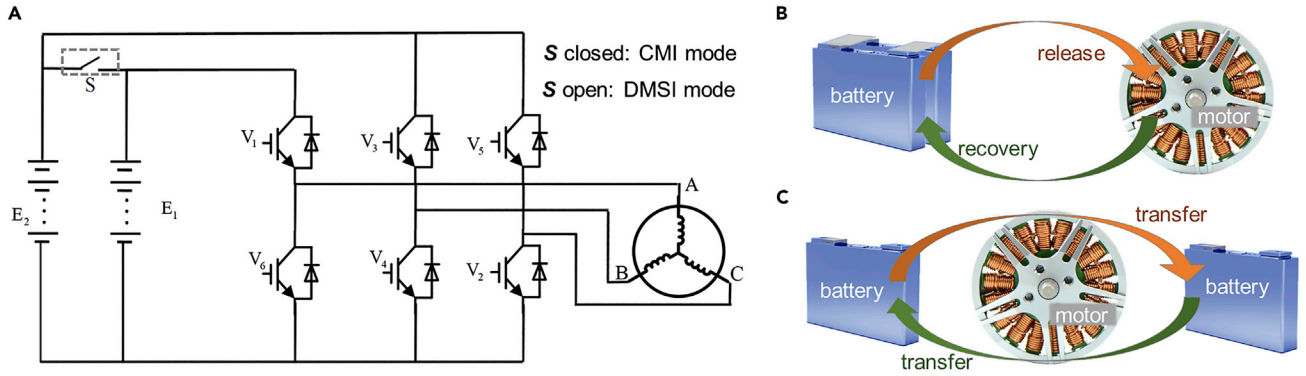

Figure 1. Schematic of the designed drive circuitry and achievable operation modes for battery heating

(A) Proposed drive circuitry, in which rapid heating of the battery pack is possible. The circuitry is equivalent to an existing circuitry if *S* is closed (CMI mode). If *S* is open, the circuitry operates in the DMSI mode.

(B) Scheme of battery heating in the CMI mode, in which the energy is transmitted between the battery and the motor.

(C) Scheme of battery heating in the DMSI mode, in which the energy is transferred between different battery modules through the motor.

cathode and anode, and heat is generated due to the ohmic resistance and electrochemical reaction (Zhang et al., 2015). Furthermore, research has been conducted to optimize the principle of AC to achieve the maximum heating performance (Ge et al., 2016; Jiang et al., 2018; Li et al., 2019a; Qin et al., 2020). However, one demerit of this method is the generation of AC, whose behavior cannot be comprehended as the equipment for laboratory research, such as Autolab, cannot reproduce its effect on a battery pack of an EV. This problem can be mitigated by generating AC with the charging station (Zuniga et al., 2015). However, this station puts burdens on the infrastructure, and is only available during charging. Meanwhile, certain on-board circuits, such as the heat-balancing topology (Shang et al., 2018), an integrated heater-equalizer (Shang et al., 2019), or resonant circuits (Shang et al., 2020), have been proposed to realize battery heating under any condition. However, these circuits inevitably add additional electronic components to EVs, resulting in bulky size and high cost. A cost-effective alternative to this method is the generation of AC using the on-board drive circuitry of the motor (Stuart and Hande, 2004). However, the temperature rise achieved in this method is not sufficiently fast.

This study first explores the reasons for inadequate heating currents generated by the existing drive circuitry on EVs. Then, a refined circuitry topology, which leads to the cost reduction of battery heating and exhibits good compatibility with the existing circuit, and an operation method for improving the heating currents with electricity transferred between cells, which is theoretically and experimentally validated, are proposed. These experiments evaluate the heating speed, efficiency, and degradation of the battery under the application of the proposed operation method. Finally, rapid, efficient, and non-detrimental battery heating is achieved using the proposed drive circuitry on EVs.

Results

Innovative topology of the drive circuitry

In the existing drive circuitry of EVs, the motor can motivate the energy release and recovery of the battery; therefore, the battery is heated under pulse currents, due to electricity exchange between the battery and motor. In contrast, the proposed drive circuitry, which is composed of two individual modules connected to the separated bridges of the invertor, is illustrated in Figure 1A. Each module comprises cells connected in series to reach the bus voltage of the inverter. The first bridge of the inverter is connected to the first module, while the remaining bridges are connected to the second module. Evidently, the currents of these modules remain independent, unless switch *S* is closed. In the case with *S* closed, each module is connected in parallel and the system configuration is identical to that of an existing drive circuitry. The proposed circuitry is, therefore, easy to implement and highly compatible with the currently used drive circuitry in EVs. The modification of the topology adds limited costs with the addition of a relay, the corresponding control circuits, and the process of battery grouping, when compared with the existing circuitry.

The proposed drive circuitry can realize two operation modes depending on the state of switch *S*. When *S* is closed (parallel configuration), the battery pack is directly charged and heated by the stored energy

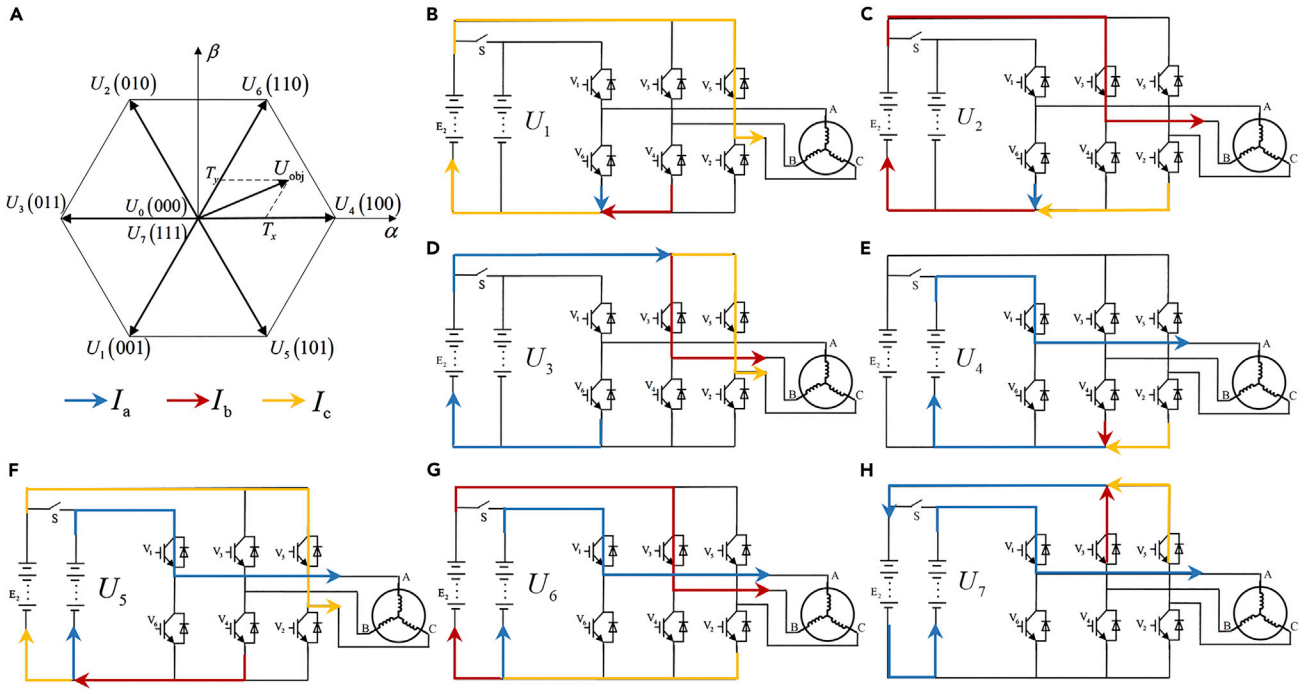

Figure 2. Voltage vectors and currents in the DMSI mode

(A) Eight switch states of the inverter (000, 001, 010, 011, 100, 101, 110, and 111) and their corresponding voltage vectors (U_0, U_1, U_2, U_3, U_4, U_5, U_6, and U_7) in the FOC of the motor.

(B–H) Currents in the drive circuitry considering different voltage vectors in the DMSI mode. The phase currents, I_a, I_b, and I_c are indicated by the blue, red, and yellow lines, respectively. The current under U_0 is not displayed as no currents are transmitted to the batteries under this condition.

provided by the motor coils, as shown in Figure 1B. Given that the currents of the motor are inverted from those of the paralleled battery modules, this heating method is called the combined module invert (CMI) mode in this article. In contrast, when *S* is open, the battery heating can also be achieved with one module charged while the other is discharged (Figure 1C), therefore enhancing the robustness of the proposed method. Assuming that the currents of the motor are inverted from those of the individual modules, this method is referred to as the dual-module separated invert (DMSI) mode in this article.

The battery currents are higher if the drive circuitry is in the DMSI mode, when compared with those generated in the CMI mode. To illustrate the improvement in the heating performance in the DMSI mode, the battery currents are calculated based on the switch states of the inverter. A total of eight states, which correspond with the base vectors in the field-oriented control (FOC) of motors (Kazmierkowski and Malesani, 1998), of the inverter are evaluated: 000, 001, 010, 011, 100, 101, 110, and 111. Figure 2A illustrates the mapping from the inverter states to the voltage vectors, which includes six base effective vectors (U_1, U_2, U_3, U_4, U_5, and U_6) and two zero-voltage vectors (U_0, and U_7). In the DMSI mode, all voltage vectors, except U_0, result in a state in which the coil currents are transmitted from the motor to the battery module, as shown in Figures 2B–2H. The amplitude of each module current is calculated and compared with that of the corresponding state in the CMI mode, as outlined in Table 1. The total heating power under the base effective vectors in the DMSI mode is approximately twice that in the CMI mode. Furthermore, for the zero-voltage vector U_7, the DMSI mode transmits the a-phase current of the motor to the batteries, in contrast with the no current transmission in the CMI mode. Under this condition of the DMSI mode, the current of battery module 1 is opposite to that of module 2, therefore, the electricity released by one module is transferred to the other.

Heat is generated when the currents flow through the battery, inverter, and motor, owing to the Joule effect. In the DMSI mode, a higher current of battery, due to the electricity transfer between the modules, can polarize the battery larger and generate more heat inside the cells considering identical motor currents. Therefore, a faster transient regime of the heating process is expected.

Vector	S_a	S_b	S_c	DMSI mode			CMI mode		
				I_1	I_2	$I_1^2 + I_2^2$	I_1	I_2	$I_1^2 + I_2^2$
U_0	0[a]	0	0	0	0	0	0	0	0
U_1	0	0	1[a]	0	i_c	i_c^2	$i_c/2$	$i_c/2$	$i_c^2/2$
U_2	0	1	0	0	i_b	i_b^2	$i_b/2$	$i_b/2$	$i_b^2/2$
U_3	0	1	1	0	$-i_a$	i_a^2	$-i_a/2$	$-i_a/2$	$i_a^2/2$
U_4	1	0	0	i_a	0	i_a^2	$i_a/2$	$i_a/2$	$i_a^2/2$
U_5	1	0	1	i_a	i_c	$i_a^2 + i_c^2$	$-i_b/2$	$-i_b/2$	$i_b^2/2$
U_6	1	1	0	i_a	i_b	$i_a^2 + i_b^2$	$-i_c/2$	$-i_c/2$	$i_c^2/2$
U_7	1	1	1	i_a	$-i_a$	$2i_a^2$	0	0	0

Table 1. Voltage vectors in motor control, the corresponding switch states of the three bridges of the inverter (S_a, S_b, and S_c), and the current of each module (I_1 and I_2) under the CMI and DMSI modes

[a]The switch state of the top transistor closed and bottom transistor open is represented by 1, and the vice versa is represented by 0.

Constraints on circuit operation and heat power of batteries

The execution of the battery heating process with the drive circuitry must comply with the operating limits of EVs. For a passenger EV, whose parameters are outlined in Table 2, the motor speed, inverter voltage, and the coil currents must be constrained during the heating procedure.

Motor operating in static mode

Generally, battery heating is only executed before charging or driving an EV, when its speed is zero and the electrical angle of the drive motor, θ, is constant. An effective solution for the static motor is the zero-torque output, which is obtained when appropriate d- and q-axis currents, i_d and i_q, are provided to the FOC system, which can be expressed as:

$$i_q = 0 \quad \text{(Equation 1)}$$

$$T_e = \frac{3}{2} p\left[\psi_f + \left(L_d - L_q\right) i_d\right] i_q = 0 \quad \text{(Equation 2)}$$

Voltage limited by the inverter

The target currents i_q and i_d are realized by controlling the q- and d-axis voltage, u_q and u_q of the rotating axis system:

$$\begin{cases} u_q = 0 \\ u_d = R_s i_d + L_d \dfrac{di_d}{dt} \end{cases} \quad \text{(Equation 3)}$$

In FOC, the target voltage is represented by a mean vector—which is influenced by two neighboring base effective vectors (U_x and U_y) of the hexagonal star diagram (Figure 2A), the zero vector U_z, as well as their specified periods (T_x,T_y and T_0)—during the pulse width modulation (PWM) period (T_{PWM}). The target voltage and the T_{PWM} are calculated through Equation (4):

$$\begin{cases} \vec{U}_x \times T_x + \vec{U}_y \times T_y + \vec{U}_z \times T_0 = \left(\vec{U}_d + \vec{U}_q\right) \times T_{pwm} \\ T_x + T_y + T_0 = T_{pwm} \end{cases} \quad \text{(Equation 4)}$$

To ensure that the T_0 is positive, the target voltage needs to be constrained inside the hexagonal star diagram, as shown by Equation (5):

$$\left|\vec{U}_d + \vec{U}_q\right| \le \left|\vec{U}_m(\theta)\right| \quad \text{(Equation 5)}$$

where the constrained voltage, U_m, is the maximum voltage inverted from the battery through the inverter.

Parameter	Symbol	Value
Battery pack	N	110S2P
Cell nominal voltage	V_{cell}	3.7 V
Cell capacity	C_{cell}	50 Ah
Ambient temperature	T_{∞}	−7°C
Drain-source resistance of IGBT	R_{I}	1.6 mΩ
Rated voltage of invertor	U_{m}	650 V
Inductance of direct axis	L_{d}	0.38 mH
Inductance of quadrature axis	L_{q}	1.065 mH
Line resistance	R_{L}	15.4 mΩ
Rated power	P_{n}	60 kW
Rated line current	I_{n}	130 A
Maximum line current	I_{m}	200 A
Pole pairs	p	4
Flux linkage	ψ_{f}	0.19 V·s

Table 2. Parameters of the heating system used in the experiments
IGBT, insulated gate bipolar transistor.

Current limited by the motor coil

The motor phase currents can be derived from the d-axis current by an inverse Park-Clarke transform (Pillay and Krishnan, 1989):

$$\begin{bmatrix} i_a \\ i_b \\ i_c \end{bmatrix} = f_{2r3s}(\theta)\begin{bmatrix} i_d \\ i_q \end{bmatrix} = \begin{bmatrix} \cos\theta \\ \cos\left(\theta - \frac{2}{3}\pi\right) \\ \cos\left(\theta + \frac{2}{3}\pi\right) \end{bmatrix} i_d \quad \text{(Equation 6)}$$

To avoid overheating of the motor coils and inverter, the root-mean-square (RMS) of the phase current should be lower than the permitted motor current I_m, as expressed by Equation (7):

$$\max\{I_{Arms}, I_{Brms}, I_{Crms}\} \leq I_m \quad \text{(Equation 7)}$$

Heat power of batteries

The heating power of the batteries can be calculated based on Joule's law:

$$P_{heat} = I_{eff\_B}^2 R_{bat} \quad \text{(Equation 8)}$$

where the battery resistance, R_{bat}, is negatively affected by the temperature (Zhang et al., 2004) and the current frequency in AC heating. Generally, high-frequency currents result in a low resistance, and vice versa (Zhang et al., 2015). The equivalent heating current, I_{eff_B}, generated by the circuits, can be calculated with the RMS of the battery currents, as shown in Equation (9):

$$I_{eff\_B}^2 = \frac{1}{T_p}\int_0^{T_p}\left(\frac{T_x}{T_{pwm}}i_x^2 + \frac{T_y}{T_{pwm}}i_y^2 + \frac{T_0}{T_{pwm}}i_0^2\right)dt \quad \text{(Equation 9)}$$

where T_p is the period of heating currents on batteries, which are influenced by the phase currents of the motor.

To increase the heating speed—I_{eff_B}, which is influenced by the electrical angle, θ, period of the d-axis current, T_p, and waveform of the d-axis current, i_d(t)—needs to be maximized considering the CMI and DMSI modes within the constraints described by Equation (1, 5, and 7), as represented by Equation (10).

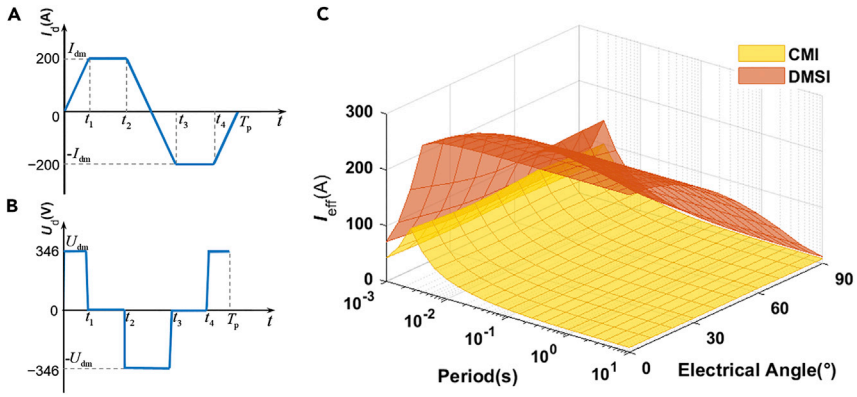

Figure 3. Battery heating currents in the DMSI and CMI modes

(A and B) Typical d-axis current and corresponding d-axis voltage of the motor.

(C) Resultant heating currents on batteries in the DMSI and CMI modes, based on periods and electrical angles. U_7 is used as the zero-voltage vector in the DMSI mode to achieve rapid battery heating.

$$\begin{cases} \max I_{eff\_B}(x) \\ x = \left[\theta, T_p, i_d(t)\right]^T \end{cases} \quad \text{(Equation 10)}$$

Comparison of the heat currents provided in each mode considering identical motor currents

The heating currents of the circuitry can be improved in the DMSI mode, due to the higher battery currents, i_x and i_y, at the base effective vectors, and the emerging current, i_0, at the zero vector U_7.

Figure 3 shows I_{eff_B} obtained with the DMSI and CMI modes under a typical operation condition of the motor within the previously discussed constraints. The torque constraints are satisfied when the current and voltage on the q-axis are zero. In contrast, the current constraints are fulfilled when the maximum d-axis current shows a fixed value, as shown in Figure 3A and Equation (11):

$$I_{dm} = I_m \quad \text{(Equation 11)}$$

Figure 3B illustrates the corresponding d-axis voltage, which satisfies Equation (5) because the maximum voltage shows a fixed value:

$$U_{dm} = \min(U_m(\theta)) \quad \text{(Equation 12)}$$

As a result, I_{eff_B} is determined by T_p and θ, as shown in Figure 3C. The battery heating current when the circuit is in the DMSI mode is evidently higher than that when it is in the CMI mode, especially when the heating period increases. At a high frequency, I_{eff_B} increases due to the higher battery currents influenced by the base effective vectors in the DMSI mode, when compared with the CMI mode. Furthermore, I_{eff_B} is approximately constant in the DMSI mode and decreases in the CMI mode when the frequency decreases. This behavior is influenced by the emerging battery currents corresponding to the zero vector U_7 in the DMSI mode (Table 1). It is worthy to note that the heating currents in the DMSI and CMI mode are sensitive to the electrical angle and period, respectively. In particular, I_{eff_B} decreases from 277 A to 48 A in the DMSI mode when the electric angle increases from 0° to 90° at a period of 0.01s for i_d(t). In contrast, I_{eff_B} drops from 108 A to 9 A in the CMI mode when the period of i_d(t) increases from 0.0025 to 1 s at the electric angle of 0°. Therefore, the best parameter conditions need to be searched to obtain the maximum heating performance in each mode separately.

Limited maximum heating currents in the CMI mode

Here, the battery heating currents achieved in the CMI mode is calculated, to compare with that achieved in the DMSI mode. In the CMI mode, the energy storage and release of the motor coil result in the pulse discharge and charge of the battery. The maximum currents of the battery heating are analyzed on EVs with the parameters outlined in Table 2, resulting in a maximum I_{eff_B} of 70.4 A and a corresponding pulse current of 1.41C on each cell, in the CMI mode, when T_p and θ are optimized to 0.008 s and 90° (or 30°/150°/210°/270°/330°) respectively.

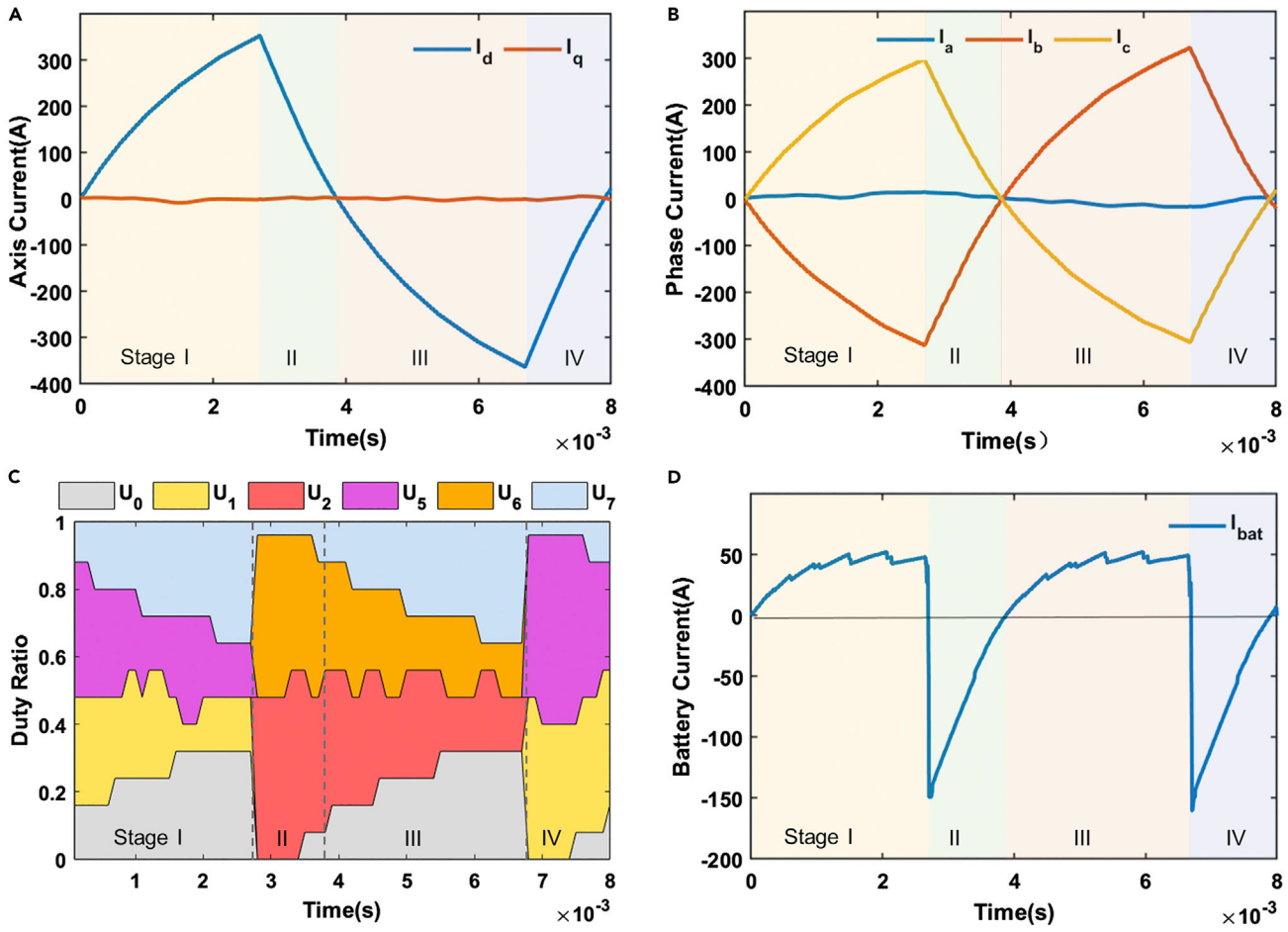

Figure 4. Optimized operation conditions for achieving the highest effective currents of battery heating in the CMI mode

(A) The d- and q-axis currents of the motor realizing a zero-torque output.

(B) Phase currents, which are constraint by the maximum permitted currents of the coils.

(C) Composition of variable voltage vectors during a single heating period.

(D) Behavior of the current of a single cell.

The d- and q-axis currents of the motor, under the constrained voltage, at this optimal operating point are illustrated in Figure 4A. The q-axis current is maintained at zero to realize a zero-torque output, ensuring that the rotors remain in a stationary state. The behavior of the d-axis current is similar to that of a triangular wave whose maximum value is 350 A. The corresponding phase currents of the motor are depicted in Figure 4B, where the RMS of the b- and c-phase currents of the motor simultaneously reach the maximum allowable value (200 A). The currents of the motor coils are controlled by FOC, which determines the switch states of the inverter. Meanwhile, once the inverter switches are closed, the phase currents are transmitted to the battery according to the current distribution stated in Table 1; therefore, I_{eff_B} for the batteries is determined by the duty ratio of all switch states, namely, the composition of base voltage vectors (Figure 4C). The behavior of the battery heating currents, as depicted in Figure 4D, can be decomposed into four stages for a heating period, which is summarized in Table 3.

Stage I: The voltage vectors U_0, U_1, U_5, and U_7 are dominant. The phase currents I_c and $-I_b$ are transmitted to the batteries due to U_1 and U_5, respectively. In contrast, no current flows through the batteries when U_0 and U_7 influence the circuit. As a result, the pulse currents of the batteries are smaller than the phase currents of the motor.

Stage II: The voltage vectors U_0, U_2, U_6, and U_7 are dominant. The currents I_b and $-I_c$ are alternately transmitted to the batteries when U_2 and U_6 are alternately applied. The operating times of the zero-voltage

	Voltage vectors	Proportion ratio	Current of battery pack
Stage I	U_1	22.8%	i_c
	U_5	25.5%	$-i_b$
	U_0 or U_7	51.7%	0
Stage II	U_2	48.5%	i_b
	U_6	41.9%	$-i_c$
	U_0 or U_7	9.6%	0
Stage III	U_2	25.8%	i_b
	U_6	21.7%	$-i_c$
	U_0 or U_7	52.5%	0
Stage IV	U_1	41.7%	i_c
	U_5	47.5%	$-i_b$
	U_0 or U_7	10.8%	0

Table 3. The composition of voltage vectors and the resulteing battery currents at each stage in the CMI mode

vectors U_0 and U_7 are relatively shorter than that in stage I (Figure 4C and Table 3); therefore the amplitudes of the heating currents of the batteries are larger, and more approximate to the motor phase currents.

Stage III: The composition of the voltage vectors is same as that in Stage II; however, the effective times of U_0 and U_7 are longer. As a result, the amplitude of battery heating current is lower than that in stage II.

Stage IV: The composition of the voltage vectors is same as that in Stage I; however, the effective times of U_0 and U_7 are shorter. As a result, the amplitude of battery heating current is higher than that in stage I.

In the CMI mode, the heating currents of the battery pack are limited by the amplitude of the motor currents and the proportion of the effective vectors in the inverter control. Moreover, the motor currents cannot be transmitted to the batteries during the zero-voltage vectors act. Therefore, the maximum I_{eff_B} of the battery pack can only be equivalent to a pulse current of 1.41C with a heating period of 0.008 s.

By increasing the heating period, the proportion of the zero-voltage vector increases, resulting in decrease of the equivalent heating currents. Figure S1 shows the operating conditions and current behaviors for the maximum heating currents when the heating period was 0.06 s. Under this condition, an increased amplitude of the coil currents (see Stage I in Figure S1B) was observed, followed by a zero current (see Stage II in Figure S1B) to maintain the RMS of coil current within the allowable value. The battery currents were negligible during the zero-current flowed in the motor coils (see Stage II in Figure S1D). Influenced by the rest time of battery, the RMS of the heating currents dropped to 0.98C after optimization. Therefore, the I_{eff_B} is negatively influenced when the heating period is prolonged. This characteristic of the traditional CMI mode is unfavorable for the LIB heating, where a faster temperature rise rate under low-frequency pulse currents is obtained.

Higher heating currents in the DMSI mode

Battery heating in the DMSI mode is realized due to the energy storage and release of the motor coil, together through the electricity transfer between different battery modules, obtained with U_7, which does not transmit any current to the batteries in the CMI mode. In addition, the currents flowing through the batteries are higher in the DMSI mode when the base effective vectors, U_1, U_2, U_3, U_4, U_5, and U_6, take effect with identical currents of the motor coil.

The maximum heating currents of the batteries in the DMSI mode are analyzed under the same constraints (see Table 2) as those in the CMI mode. The longer heating period, 0.06s, which leads to a

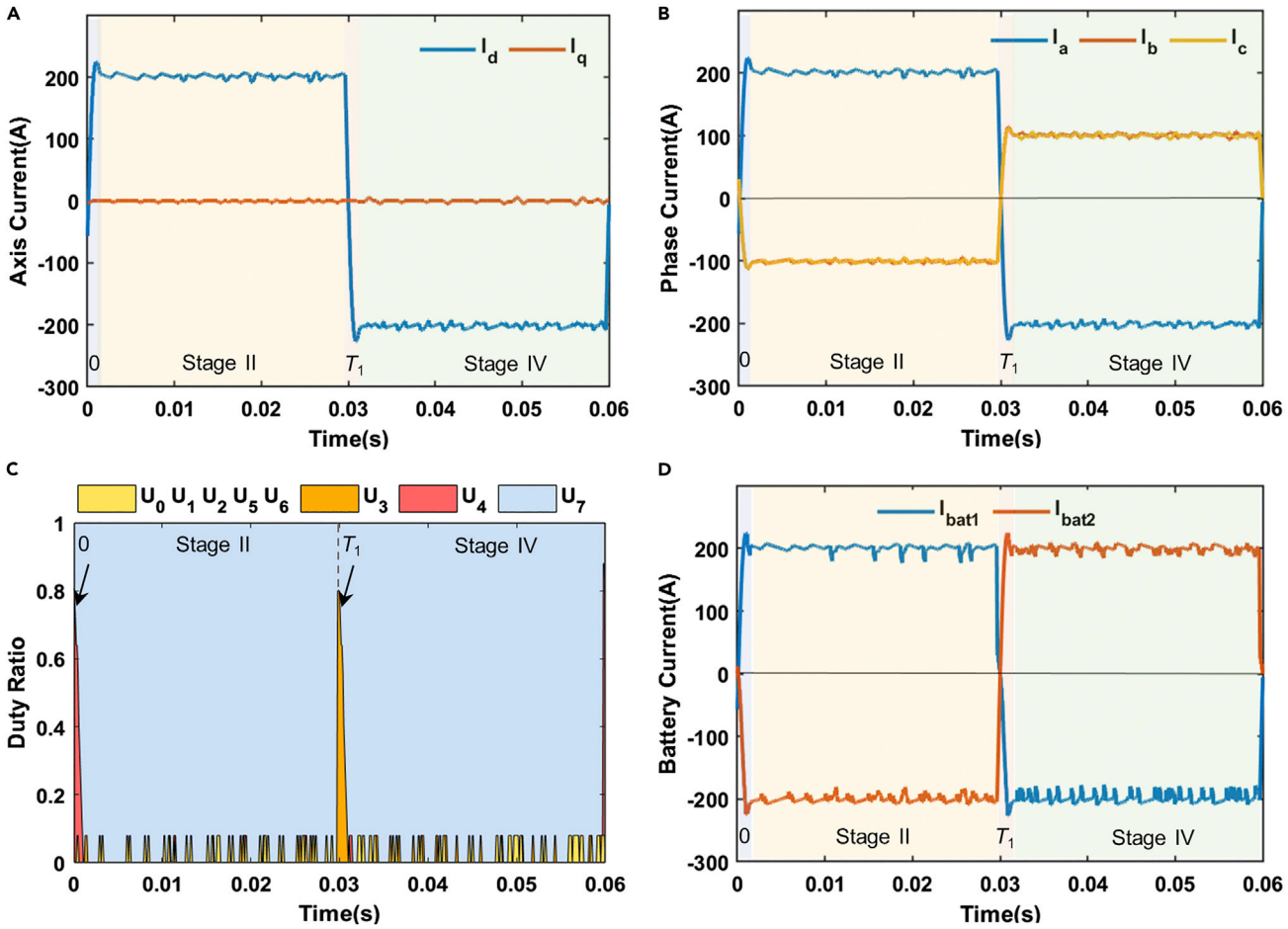

Figure 5. Optimized operation conditions in the DMSI mode considering a period of 0.06 s

(A) The d- and q-axis currents of the motor, resulting in a zero-torque output under the constrained voltage.

(B) Phase currents of the motor.

(C) Composition of variable voltage vectors.

(D) Currents flowing through battery modules 1 and 2.

maximum heating current of 0.98C in the CMI mode is adopted in the DMSI mode to compare the battery heating currents. After the operation is optimized, a maximum battery heating current of 199 A (3.98C) is obtained with an electrical angle of 0° (or 180°). In this case, the q-axis current of the motor is zero to ensure a stationary state rotor of the motor, whereas the behavior of the d-axis and phase currents resembles that of a square wave (Figures 5A and 5B). The RMS of the a-phase current is 200 A, which is the highest allowable value. Meanwhile, the composition of the base vectors is shown in Figure 5C. The resultant battery currents include two steady and two transition stages, as indicated in Figure 5D and summarized in Table 4.

Stage I ($t = 0$): In this first transient stage, U_4 is the dominant vector and the d-axis current increases from 0 to 200A. The amplitude of the current of battery module 1 is similar to I_a, owing to U_4.

Stage II ($0 < t < T_1$): In this first steady stage, U_7 is dominant and the motor current is constant, whereas the proportion of the other base vectors is negligible. As a result, the current of module 1 is equal to I_a, and opposite to that of module 2. Thus, the electricity is transferred from module 1 to 2.

Stage III ($t = T_1$): In this second transient stage, the base vector U_3 is dominant, resulting in a decrease in the d-axis current from 200 A to −200 A. Meanwhile, the amplitude of the current of battery module 2 is close to I_a, whereas the direction is reverse, due to U_3.

	Current characteristics	Voltage vectors	Proportion ratio	Current of module 1	Current of module 2
Stage I	Current direction adjustment	U_4	53.8%	i_a	*0*
		U_7	43.7%	i_a	$-i_a$
		others	2.5%		
Stage II	Module 1 discharged; module 2 charged	U_7	97.8%	i_a	$-i_a$
		Others	2.2%		
Stage III	Current direction adjustment	U_3	53.8%	*0*	$-i_a$
		U_7	46.1%	i_a	$-i_a$
		Others	0.1%		
Stage IV	Module 1 charged; module 2 discharged	U_7	97.0%	i_a	$-i_a$
		Others	3.0%		

Table 4. Composition of voltage vectors and the resulting battery currents at each stage in the DMSI mode

Stage IV ($T_1 < t < T_p$): In this second steady stage, U_7 is dominant and the motor current is constant. As a result, electricity is transferred from module 2 to 1.

The DMSI mode can, therefore, ensure the energy transfer between modules 1 and 2, resulting in substantially increased heating currents of the battery pack. In this mode, the equivalent heating currents are 280% of the maximum value obtained in the CMI mode.

In addition, these heating currents can be maintained when the drive circuitry operates under a longer period in the DMSI mode. In particular, a battery heating current of 200A (4C) is achieved when the operation period is 1.6 s (see Figure S2). In this case, the electrical angle of the motor rotor, as well as the behavior and amplitude of the coil current, is preserved; and high heating currents are realized at low frequency due to the high proportion ratio of U_7. A further increase in the heating speed of batteries is, therefore, expected due to the higher battery resistance under a low-frequency pulse current (Zhang et al., 2015).

The maximum heating currents of the batteries in the DMSI mode are sensitive to the size of the battery pack and motor. Therefore, different motor power and battery energy, besides those listed in Table 2, are evaluated in battery heating with the DMSI mode. The RMS values of battery currents are positively affected by motor power, as illustrated in Figure 6, because of the higher allowable currents in the drive circuitry with increased motor power. In contrast, those RMS values are negatively affected by battery energy, as lower pulse rates on batteries result with the decreased battery capacity. Even so, a pulse current of 4C is achievable with a motor-power-to-battery-energy ratio higher than 1.5 h^{-1}, which can be satisfied in most passenger EVs.

Temperature rise, heating efficiency, and capacity degradation

The rate of temperature rise of cells heated by the pulse currents, which are generated from the drive circuitry at an ambient temperature of −7°C (see Transparent methods and Figure S6), is illustrated in Figure 7A. In the DMSI mode, the resultant pulse current (4C) leads to mean temperature rates of 4.8 and 7.2°C/min in 5 min under the pulse periods of 0.06 and 1.6 s, respectively. The temperature rate is, therefore, positively affected by the heating period, even though the amplitude of the pulse currents is constant, as more electrochemical processes, such as charge transfer and ion diffusion, are involved in the heat generation due to the long-period pulse current (Zhang et al., 2015).

The DMSI mode with a pulse period of 1.6 s is focused in subsequent analysis considering the higher heating speed. The mean temperature rates are 8.6 and 8.5°C/min in the first and second minutes, respectively, and 6.3°C/min in the remaining 3 minutes. A decrease in the mean temperature rate is observed during the heating process as the battery impedance decreases with the temperature (Zhang et al., 2004). However, the temperature rate, especially at the initial stage, is sufficient to result in rapid battery heating in a cold environment.

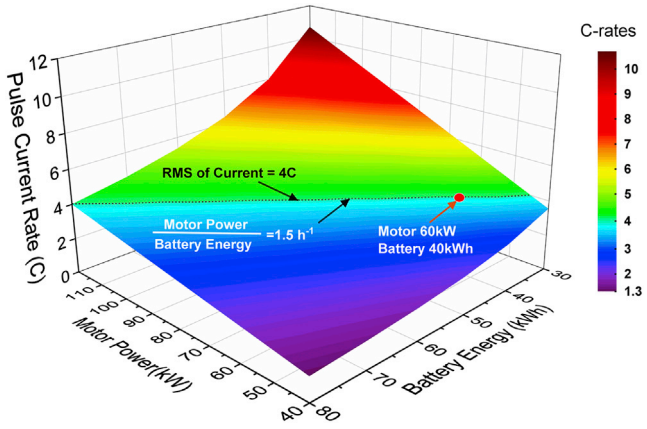

Figure 6. Maximum heating currents in the DMSI mode with motor power and battery energy
The conditions resulting in a pulse current of 4C are shown with the dashed line in the map.

Meanwhile, a high heating efficiency is also achieved in the DMSI mode. Figure 7B shows the proportion of heat generation in different components, considering a pulse period of 1.6 s. The heat generation in the battery pack (Q_{bat}) accounts for most of the total heat (97.7%), as the low-temperature internal resistance of the batteries is significantly higher than those of the motor and inverter. Furthermore, the heat dissipated from the batteries (Q_{dis}) corresponds to a small portion of the total heat (8%), as the heat is generated internally and time for dissipation is limited. Therefore, the efficiency of this heating process reaches 89.7% during the temperature rise from −7°C to 29.1°C. The energy of battery heating is converted from the voltage polarization of cells during charging and discharging (see Figure S3). The discharged capacity is higher than the charged capacity. Therefore, the discharged energy of the battery is partly converted to heat, whereas the rest is restored in the battery. A capacity of 2.5 Ah, corresponding to 4.9% of the nominal capacity, is lost and converted to heat for each cell in this proposed method for heating. It is worth noting that the heating efficiency of the drive circuitry is also influenced by the heat transfer coefficient of the cells in the battery pack, which determines the heat loss from the warm cells to cold accessories in the heating process. In this study, the heat transfer coefficient of cells in a thermal chamber (9.6 W/(m^2·K), see Table S1) was adopted in the calculation of heating efficiency. Furthermore, the value of heating efficiency and capacity loss may slightly deviate from those of the real battery pack.

The heating performance of the drive circuitry is influenced by the initial temperature; therefore, experiments are performed at a lower ambient temperature of −16°C (see Figure S5). Lower temperature increases the battery resistance. In this case, the RMS of battery currents decreases to 190 A (3.8 C); however, the temperature rate of cells increases due to the higher resistance and larger voltage polarization, even though the coil currents remain the same. Temperature rises of 9.9°C/min and 8.2°C/min are obtained at the first minute and during the whole process, respectively. Correspondingly, a higher capacity loss (2.9 Ah) corresponding to 5.8% of the nominal capacity, is resulted in the heating process.

Battery degradation during the heating process may be caused by the internal side reactions, which are accelerated if the current pulses are long and large, resulting in a decrease in the usable capacity (Han et al., 2019). The degradation of cells in module 1 and 2 are same, because of their identical operation condition involving charging and discharging alternatively. Thus, the capacity change in a single cell after heating in the DMSI mode (T_p = 1.6 s, from −7°C to 29.1°C) is recorded, as shown in Figure 7C. After 5,000 cycles, the faded capacity is 0.5%. Besides, the disassembled anode from this faded cell involves neither gray materials on the optical photograph nor mossy materials on the scanning electron microscopic image, indicating the absence of lithium plating (see Figure S4). Therefore, the effect of the proposed heating process on battery degradation is negligible.

Discussion

This study analyzed the heating currents generated by an existing drive circuitry of EVs (CMI mode), where a maximum heating current of 1.4C was obtained for the batteries. Furthermore, the heating currents

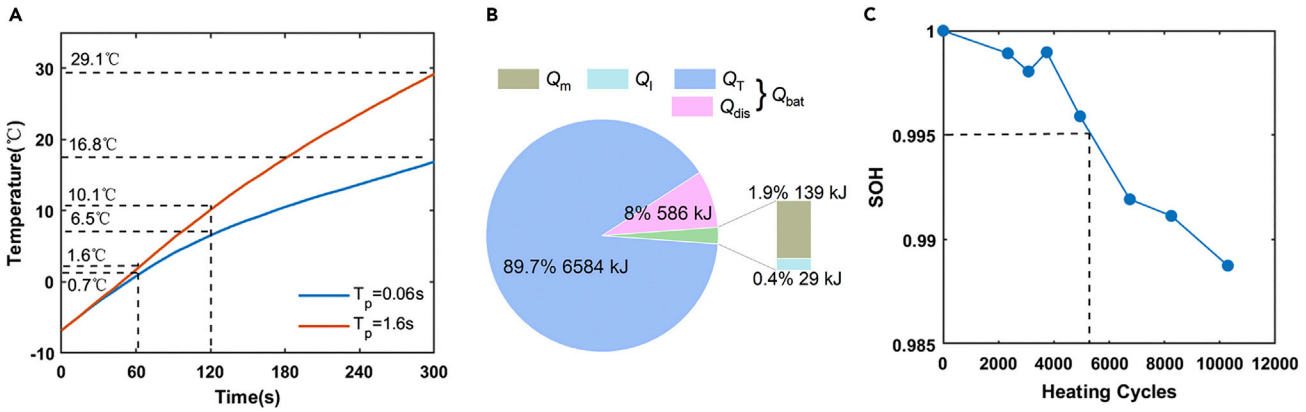

Figure 7. Battery heating and degradation in the DMSI mode

(A) Battery temperature during first 5 min (300s) of the heating process at an ambient temperature of −7°C, considering heating periods of 0.06 and 1.6 s.
(B) The composition of total heat generation, considering a period of 1.6 s, including heat generated in batteries (Q_T and Q_{dis}), motor (Q_T), and inverter (Q_I).
(C) The capacity degradation of the battery is based on heating cycles.

decreased with the heating period, owing to the limited ability of energy storage in the motor coil and the zero-voltage vectors of the inverter control. This characteristic is unfavorable for the LIB heating, where a faster temperature rise rate is obtained under low-frequency pulse currents, therefore degrading the heating performance.

A refined topology configuration, in which the cells were rearranged into two modules and a relay was added, was proposed to increase the heating speed. With this configuration, a new operation mode (DMSI mode) was achieved, where the heating currents of the batteries emerged when the inverter is at the zero-voltage vector, enabling electricity transfer between the modules.

The result of the theoretical analysis showed that the battery heating currents under the identical operation condition of the motor were improved in the DMSI mode. Furthermore, an equivalent heating current of 4C was obtained under variable heating periods with the prototype experiments of a passenger EV. At an ambient temperature of −7°C, the mean temperature rates of the battery pack at the start of the heating and during the whole process were 8.6°C/min and 7.2°C/min, respectively. A high heating efficiency (>80%) and negligible battery degradation (0.5% after 5,000 cycles) were also obtained.

Improved heating performance of the battery pack was, therefore, obtained with the proposed driving circuitry and the DMSI operation mode. Moreover, it was compatible with the existing driving circuits with the CMI mode. This study provides a practical and promising solution for realizing the rapid heating of battery packs of EVs in a cold environment.

Limitations of the study

As the investigation of the heating performance of the batteries, coupled with the proposed drive circuitry, was desired in this study, only the battery heating currents, temperature rates, and capacity degradation were experimentally and theoretically evaluated. However, the impact of noise and vibration during the heating process in the implementation of the proposed drive circuitry on EVs also need to be analyzed in future work.

Resource availability

Lead contact

Further information and requests for resources and reagents should be directed to and will be fulfilled by the Lead Contact, Minggao Ouyang (ouymg@tsinghua.edu.cn).

Materials availability

This study did not generate new unique reagents.

Data and code availability

The published article includes all [datasets/code] generated or analyzed during this study.

Methods

All methods can be found in the accompanying Transparent Methods supplemental file.

Supplemental information

Supplemental Information can be found online at https://doi.org/10.1016/j.isci.2020.101921.

Acknowledgments

This work is supported by the National Natural Science Foundation of China (Grant No. 51807108) and funded by Ministry of Science and Technology of the People's Republic of China (Grant No. 2019YFE0100200).

Author contributions

Conceptualization, Y.L. and D.G.; Methodology, Y.L.; Investigation, Y.L. and Y.Q.; Writing – Original Draft, Y.L. and X.G.; Writing – Review & Editing, Y.L. and J.D.; Funding Acquisition, X.H. and M.O.; Resources, Y.L., L.L., and X.F.; Supervision, M.O.

Declaration of interests

The authors declare no competing interests.

Received: September 21, 2020
Revised: November 8, 2020
Accepted: December 4, 2020
Published: January 22, 2021

References

Figueres, C., Schellnhuber, H.J., Whiteman, G., Rockström, J., Hobley, A., and Rahmstorf, S. (2017). Three years to safeguard our climate. Nature *546*, 593–595.

Ge, H., Huang, J., Zhang, J., and Li, Z. (2016). Temperature-adaptive alternating current preheating of lithium-ion batteries with lithium deposition prevention. J. Electrochem. Soc. *163*, A290–A299.

Goodenough, J.B. (2015). Energy storage materials: a perspective. Energy Storage Mater. *1*, 158–161.

Grandjean, T., Barai, A., Hosseinzadeh, E., Guo, Y., McGordon, A., and Marco, J. (2017). Large format lithium ion pouch cell full thermal characterisation for improved electric vehicle thermal management. J. Power Sources *359*, 215–225.

Han, X., Lu, L., Zheng, Y., et al. (2019). A review on the key issues of the lithium ion battery degradation among the whole life cycle. eTransportation *1*, 100005.

Herreyre, S., Huchet, O., Barusseau, S., Perton, F., Bodet, J.M., and Biensan, P. (2001). New Li-ion electrolytes for low temperature applications. J. Power Sources *97-98*, 576–580.

Ji, Y., and Wang, C.Y. (2013). Heating strategies for Li-ion batteries operated from subzero temperatures. Electrochim. Acta *107*, 664–674.

Ji, Y., Zhang, Y., and Wang, C.-Y. (2013). Li-ion cell operation at low temperatures. J. Electrochem. Soc. *160*, A636–A649.

Jiang, J., Ruan, H., Sun, B., et al. (2018). A low-temperature internal heating strategy without lifetime reduction for large-size automotive lithium-ion battery pack. Appl. Energy *230*, 257–266.

Kazmierkowski, M.P., and Malesani, L. (1998). Current control techniques for three-phase voltage-source pwm converters: a survey. IEEE Trans. Ind. Electron. *45*, 691–703.

Li, J., Sun, D., Chai, Z., Jiang, Z., and Sun, C. (2019a). Sinusoidal alternating current heating strategy and optimization of lithium-ion batteries with a thermo-electric coupled model. Energy *186*, 115798.

Li, Y., Feng, X., Ren, D., Ouyang, M., Lu, L., and Han, X. (2019b). Thermal runaway triggered by plated lithium on the anode after fast charging. ACS Appl. Mater. Interfaces *11* (50), 46839–46850.

Li, Y., Han, X., Feng, X., Chu, Z., Gao, X., Li, R., Du, J., Lu, L., and Ouyang, M. (2021). Errors in the reference electrode measurements in real lithium-ion batteries. J. Power Sources *481*, 228933.

López-Ibarra, J.A., Goitia-Zabaleta, N., Herrera, V.I., Gazta ñaga, H., and Camblong, H. (2020). Battery aging conscious intelligent energy management strategy and sensitivity analysis of the critical factors for plug-in hybrid electric buses. eTransportation *5*, 100061.

Lu, L., Han, X., Li, J., Hua, J., and Ouyang, M. (2013). A review on the key issues for lithium-ion battery management in electric vehicles. J. Power Sources *226*, 272–288.

Pesaran, A. and Vlahinos, A. (2003). TED-AJ03-633 Cooling and Preheating of Batteries in Hybrid Electric Vehicles. https://www.semanticscholar.org/paper/Cooling-and-Preheating-of-Batteries-in-Hybrid-Pesaran-Vlahinos/9602e08e3d1a40fbc393dbc8fa1e81faf2f108a1.

Pillay, P., and Krishnan, R. (1989). Modeling, simulation, and analysis of permanent-magnet motor drives,part i: the permanent-magnet synchronous motor drive. IEEE Trans. Industry Appl. *25*, 265–273.

Qin, Y., Du, J., Lu, L., et al. (2020). A rapid lithium-ion battery heating method based on bidirectional pulsed current: heating effect and impact on battery life. Appl. Energy *280*, 115957, https://doi.org/10.1016/j.apenergy.2020.115957.

Ren, D., Hsu, H., Li, R., Feng, X., Guo, D., Han, X., Lu, L., He, X., Gao, S., Hou, J., et al. (2019). A comparative investigation of aging effects on thermal runaway behavior of lithium-ion batteries. eTransportation *2*, 100034, https://doi.org/10.1016/j.etran.2019.100034.

Shang, Y., Liu, K., Cui, N., Wang, N., Li, K., and Zhang, C. (2020). A compact resonant switched-capacitor heater for low temperatures. IEEE Trans. Power Electron. *35*, 7134–7144, https://doi.org/10.1109/TPEL.2019.2954703.

Shang, Y., Xia, B., Cui, N., Zhang, C., and Mi, C.C. (2018). An automotive onboard AC heater without external power supplies for lithium-ion batteries at low temperatures. IEEE Trans. Power Electron. *33*, 7759–7769.

Shang, Y., Zhu, C., and Fu, Y. (2019). An integrated heater equalizer for lithium-ion batteries of electric vehicles. IEEE Trans. Ind. Electron. *66*, 4398–4405.

Stuart, T.A., and Hande, A. (2004). HEV battery heating using AC currents. J. Power Sources *129*, 368–378.

Tomaszewska, A., Chu, Z., Feng, X., O'Kane, S., Liu, X., Chen, J., Ji, C., Endler, E., Li, R., Liu, L., et al. (2019). Lithium-ion battery fast charging: A review. eTransportation *1*, 100011.

Vlahinos, A. and Pesaran, A., "Energy Efficient Battery Heating in Cold Climates," SAE Technical Paper 2002-01-1975, 2002, https://doi.org/10.4271/2002-01-1975.

Waldmann, T., Hogg, B.-I., and Wohlfahrt-Mehrens, M. (2018). Li plating as unwanted side reaction in commercial Li-ion cells – A review. J. Power Sources *384*, 107–124.

Wang, C.Y., Zhang, G., Ge, S., Xu, T., Ji, Y., Yang, X.G., and Leng, Y. (2016). Lithium-ion battery structure that self-heats at low temperatures. Nature *529*, 515–518.

Wu, S., Xiong, R., Li, H., Nian, V., and Ma, S. (2020). The state of the art on preheating lithium-ion batteries in cold weather. J. Energy Storage *27*, 101059.

Xu, J., Wang, X., Yuan, N., Hu, B., Ding, J., and Ge, S. (2019). Graphite-based lithium ion battery with ultrafast charging and discharging and excellent low temperature performance. J. Power Sources *430*, 74–79.

Yang, S., He, R., Zhang, Z., et al. (2020). CHAIN: cyber hierarchy and interactional network enabling digital solution for battery full-lifespan management. Matter *3*, 27–41.

Yang, X.-G., Zhang, G., Ge, S., and Wang, C.-Y. (2018). Fast charging of lithium-ion batteries at all temperatures. Proc. Natl. Acad. Sci. U S A *115*, 7266–7271.

Zhang, J., Ge, H., Li, Z., and Ding, Z. (2015). Internal heating of lithium-ion batteries using alternating current based on the heat generation model in frequency domain. J. Power Sources *273*, 1030–1037.

Zhang, S.S., Xu, K., and Jow, T.R. (2003). The low temperature performance of Li-ion batteries. J. Power Sources *115*, 137–140.

Zhang, S.S., Xu, K., and Jow, T.R. (2004). Electrochemical impedance study on the low temperature of Li-ion batteries *49*, 1057–1061.

Zuniga, M., Jaguemont, J., Boulon, L., Dubé, Y. (2015). Heating Lithium-Ion Batteries with Bidirectional Current Pulses', 2015 IEEE Vehicle Power and Propulsion Conference, VPPC 2015 - Proceedings. https://doi.org/10.1109/VPPC.2015.7352959.

iScience, Volume *24*

Supplemental Information

Drive circuitry of an electric vehicle enabling rapid heating of the battery pack at low temperatures

Yalun Li, Xinlei Gao, Yudi Qin, Jiuyu Du, Dongxu Guo, Xuning Feng, Languang Lu, Xuebing Han, and Minggao Ouyang

Supplemental Data Items

Heating currents in the CMI mode with a prolonged period of 0.06s. Related to "Limited maximum heating currents in the CMI mode"

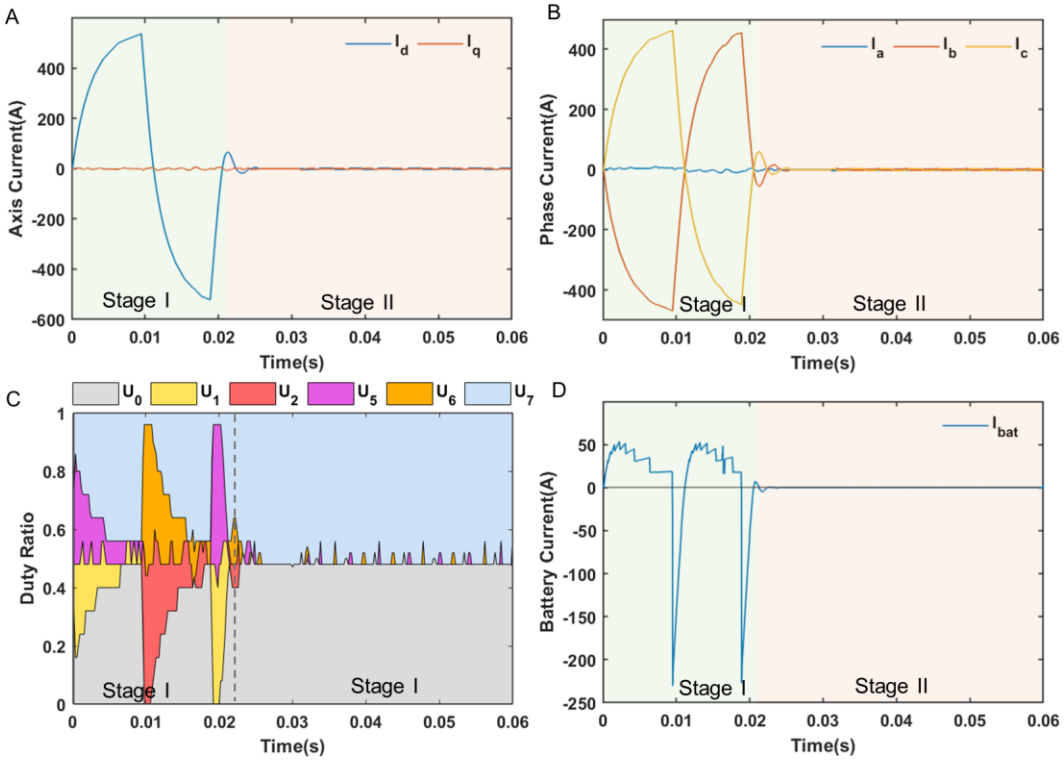

Figure S1. Decreased RMS value of battery heating currents when the heating period was increased to 0.06 s in the CMI mode. Related to Figure 4

(A) The d- and q-axis currents of the motor realizing a zero-torque output. The q-axis current resembled a triangle wave of 534A amplitude in stage I, and was zero at stage II.

(B) Phase currents, the RMS of which were maintained to an allowable value of 200A.

(C) Composition of variable voltage vectors during a single heating period. In stage I, the compositions of the voltage vectors were identical to those depicted in Fig. 4. In stage II, the voltage vectors were dominant by the zero vectors (U_0 and U_7).

(D) Behavior of the current of a single cell, with an RMS value of 49A. In stage I, the amplitude of the battery heating current was higher than that in Fig. 4. In stage II, the battery currents were negligible.

Heating currents in the DMSI mode with a prolonged period of 1.6s. Related to "Higher heating currents in the DMSI mode"

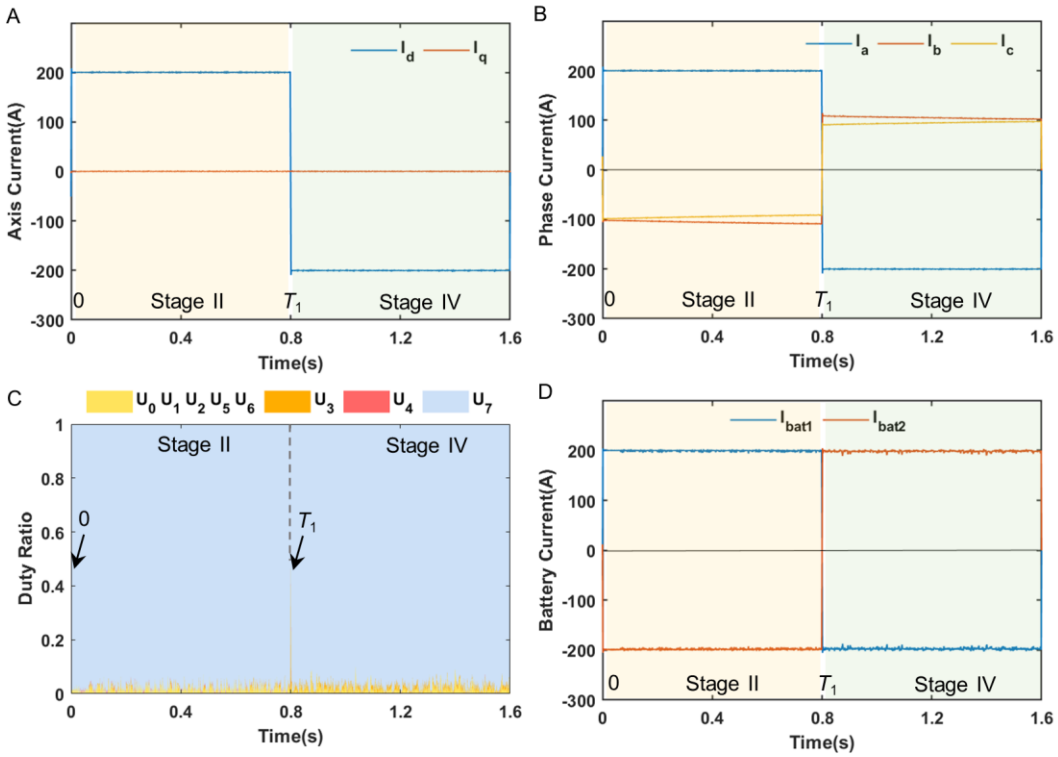

Figure S2. Optimized operation conditions in the DMSI mode considering a period of 1.6 s. Related to Figure 5

(A) The d- and q-axis currents of the motor, resulting in a zero-torque output under the constrained voltage.

(B) Phase currents, which were constrained by the maximum permitted currents of the coils.

(C) Composition of the variable voltage vectors during a single heating period, and the increased proportion ratio of U_7 was observed compared to that in Fig. 5C.

(D) Currents flowing through battery modules 1 and 2 in a period, illustrating an extended period (compared to that in Fig. 5D) in which the electricity was transferred from one battery module to the other.

Battery polarization in the DMSI mode with a period of 1.6 s when heating from -7 °C. Related to "Temperature rise, heating efficiency, and capacity degradation"

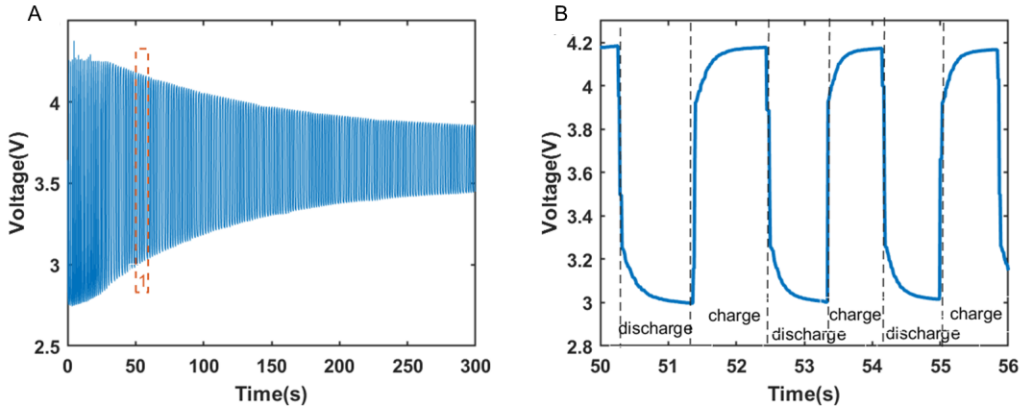

Figure S3. Battery voltage response with an initial SOC of 50% during heating at a period of 1.6 s in the DMSI mode. Related to Figure 7A and B.

(A) Cell voltage when the battery was heated from −7°C to 29.1 °C.

(B) Enlarged voltage profile of region 1 in (A), from 50 s to 56 s, illustrating the alternating charge and discharge on cells.

Battery degradation in the DMSI mode with a period of 1.6 s when heating from -7 °C. Related to "Temperature rise, heating efficiency, and capacity degradation"

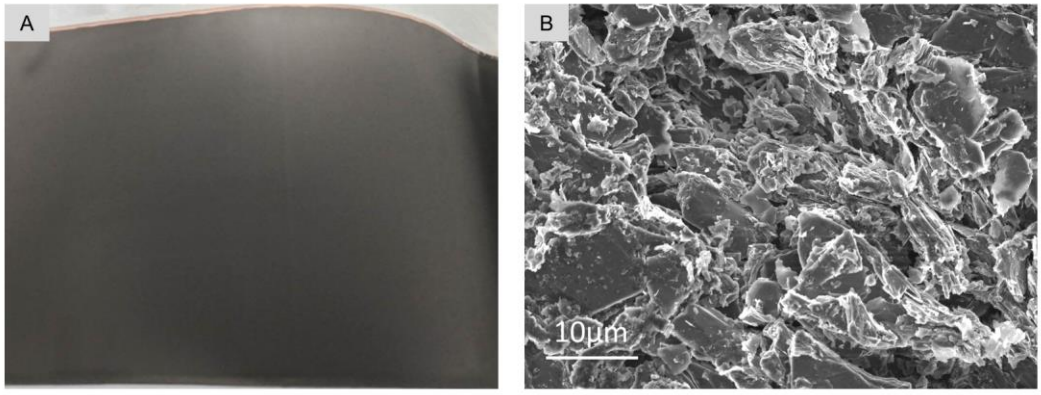

Figure S4. Optical photo and SEM image of the anode disassembled from the faded cell in the DMSI mode with a period of 1.6 s. Related to Figure 7C

(A) Optical photo of the anode, without plated gray materials on the anode surface.

(B) SEM image of the anode, illustrating no dendrites or mossy materials (indicating no lithium plating) on the graphite particles. The magnification of this image is 2000.

Battery heating performance in the DMSI mode with a period of 1.6s when heating from -16 °C. Related to "Higher heating currents in the DMSI mode" and "Temperature rise, heating efficiency, and capacity degradation"

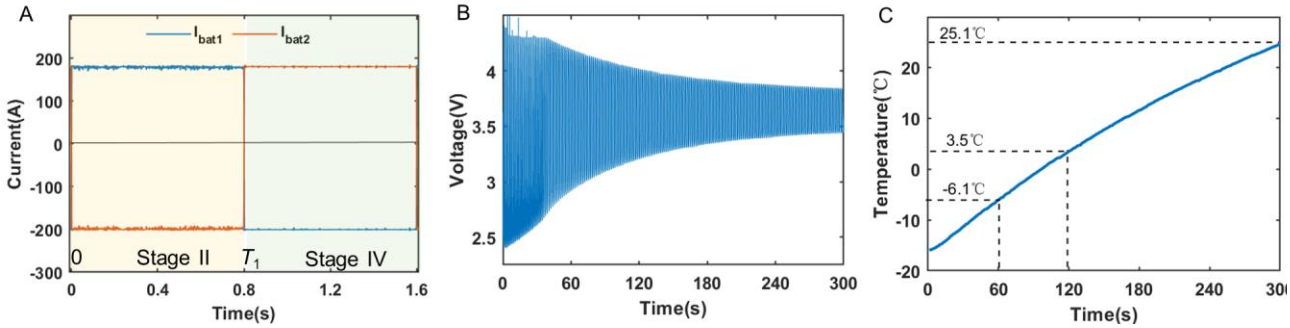

Figure S5. Battery heating from −16 °C with the proposed method (T_p = 1.6s). Related to Figure 5 and 7.

(A) Currents flowing through battery modules 1 and 2 at a period of 1.6 s, with an RMS value of 190 A (3.8C)

(B) Battery voltage response during the heating for 5 min (300 s), illustrating a larger voltage polarization than that in Fig. S3A

(C) Battery temperature increase, with the temperature rise rate of cells increasing to 9.9 °C/min and 8.2 °C/min at the first minute of heating and for the whole process, respectively

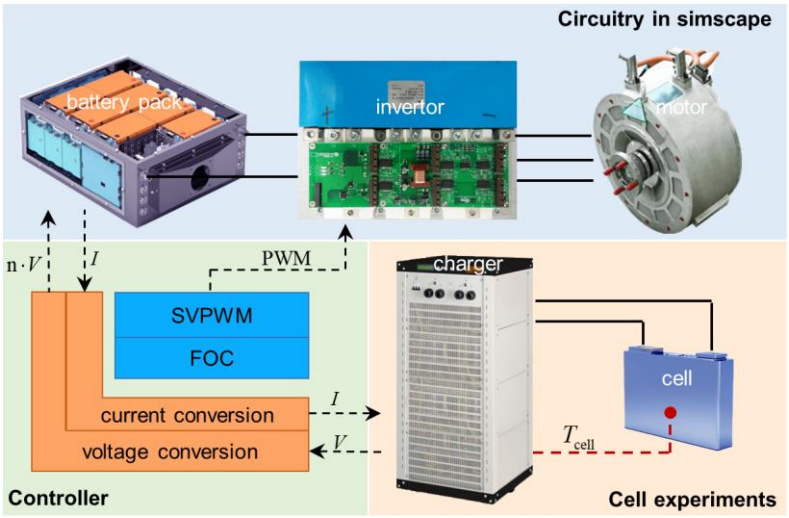

Figure S6. Setup of the prototype experiments.

The heating experiments are performed with cells charged by a charger, which tracked the current output from the inverter to the battery pack. The heating currents were obtained through simulation of the drive circuitry, including battery pack, inverter and motor, executed in real time with Simscape. The controller converted the currents of pack to cells and sent signals to indicate the charger; meanwhile, got the real-time cell voltage to the prototype in Simscape.

Transparent Methods

Experimental procedure

To test and validate the performance of the designed topology on a passenger EV integrated with LIBs, rapid prototype experiments were conducted and the equivalent equipment—including a permanent magnet synchronous motor (PMSM) with a rate power of 60 kW, a three-phase inverter with a voltage level of 650 V, as well as a battery pack with 110-series and 2-parallel cells —were developed in Simscape. At the same time, the real-time pulse currents of the battery pack obtained by the topology in the Simscape were applied in real cells by a charger. The equipment parameters are outlined in Table 2, and the experimental setup is presented in Fig. S6.

The cells used in this study had a nominal capacity of 50 Ah with a voltage range from 2.8 V to 4.2 V and an energy density of 262 Wh/kg. $Li(Ni_{0.5}Co_{0.2}Mn_{0.3})O_2$ was used as the cathode and graphite was used as the anode. The battery pack included two modules, each of which was composed of 110 cells arranged in a series string configuration. Assuming that the same pulse currents, involving alternately charging and discharging, was transmitted to each cell, the battery heating was analyzed with a single cell to obtain the equivalent temperature rise. The currents of cells were generated using a battery charger, which tracked the current output of the inverter and fed back the cell voltage to the invertor.

The PMSM used in this study was simulated in Simscape after being validated with the driving motor of a passenger EV. The inverter bridges were controlled with Space Vector Pulse Width Modulation (SVPWM)(Kumar Peddapelli, 2015), where U_7 was the only zero vector used in the experiments, due to its high currents generated on the batteries.

In the experiments, the pulse currents generated by the drive circuitry was applied to heat the fresh cells with an initial SOC of 50% in a thermal chamber at -7 °C or -16 °C. The voltage polarization and temperature increase of the cells were led to and recorded in a heating process with 5 minutes. Furthermore, the cell capacity was examined at room temperature after heating cycles to analyze the effect of the heating method on battery degradation. A cell after 5000 heating cycles was disassembled at 2.8V in the glove box, and the anode was observed with scanning electron microscopy (SEM) to inspect the lithium plating in the heating process.

Calculation of heating efficiency

The heat generated by the battery pack is the sum of the heat generated from all cells, including the heat convection loss and temperature rise of each cell(Nieto *et al.*, 2012):

$$Q_{\mathrm{bat}} = Q_{\mathrm{T}} + Q_{\mathrm{dis}} = N[cm(T - T_0) + \int hA(T - T_\infty)dt] \quad (1)$$

where Q_{T} represents the heat that results in the temperature rise of batteries, and Q_{dis} represents the heat dissipated from the batteries to the environment during the heating process. As the prototype experiment was performed on a single cell, the heat generation of the cells was multiplied by the number of cells in the battery pack.

The heat generated by the motor was obtained using Joule's law:

$$Q_{\mathrm{m}} = \int \frac{R_{\mathrm{L}}}{2}(i_{\mathrm{a}}^2 + i_{\mathrm{b}}^2 + i_{\mathrm{c}}^2)dt \quad (2)$$

Meanwhile, in the inverter operation, the turn-on loss (Eq. 3) was considered the main source of heat generation:

$$Q_{\mathrm{I}} = \int R_{\mathrm{I}}(i_{\mathrm{a}}^2 + i_{\mathrm{b}}^2 + i_{\mathrm{c}}^2)dt \quad (3)$$

The total heat generated in the drive circuitry is the sum of that in the battery pack, inverter and motor:

$$Q_{\mathrm{tot}} = Q_{\mathrm{bat}} + Q_{\mathrm{m}} + Q_{\mathrm{I}} \quad (4)$$

The heat efficiency for the heating process was calculated as the ratio of Q_{T} to Q_{tot}:

$$\eta = \frac{Q_{\mathrm{T}}}{Q_{\mathrm{tot}}} \quad (5)$$

The parameters for the calculation of heating efficiency were derived from the measurement, as listed in Table S1.

Table S1. Parameters for the heating process

Parameter	Symbol	Value
Battery Pack	*N*	220
Cell Capacity	C_{cell}	50 Ah
Cell Mass	*m*	0.738 kg
Cell Surface Area	*A*	0.0414 m^2
Battery Capacity	*c*	1126 J/(kg·K)
Initial State of Charge	*SOC*	50%
Initial State of Health	*SOH*	100%
Ambient Temperature	T_∞	-7 °C or -16 °C
Initial Cell Temperature	T_0	-7 °Cor -16 °C
Drain-source Resistance of IGBT	R_{I}	1.6 mΩ
Line Resistance	R_{L}	15.4 mΩ
Heat Transfer Coefficient	*h*	9.6 W/(m^2· K)

Please note that the heat transfer coefficient, *h*, in Table S1 was measured with cells in the thermal chamber, which is usually different from that measured in a real pack. The adoption of *h* in the thermal chamber in the calculation is because that the h value in the battery pack is unavailable. In a battery pack, additional accessories, such as a cooling plate and bus bar, are contained and absorb heat from the warm cells, as their temperature is lower than that of the cells. Here, we ignored the continuous loss of heat from cells to accessories after the preset temperature was reached (heating process stopped). In the heating process, the *h* of cells in the battery pack is positively correlated with the heat loss from the warm cells to the accessories. Therefore, the heating efficiency could decline if the *h* of the cells in the real battery pack is higher than 9.6

W/(m^2·K). For example, an *h* value of 20 W/(m^2·K) decreases the heating efficiency from 89.7% to 83% when batteries are heated from −7 °C to 29.1 °C.

Supplemental References

Kumar Peddapelli, S. (2015) '2. Space vector pulse width modulation technique', *Pulse Width Modulation*, (May). doi: 10.1515/9783110470420-002.

Nieto, N. *et al.* (2012) 'Thermal Modeling of Large Format Lithium-Ion Cells', *Journal of the Electrochemical Society*, 160(2), pp. A212–A217. doi: 10.1149/2.042302jes.